

**Climatology, seasonality and trends of oceanic coherent
eddies**

Josué Martínez-Moreno¹, Andrew McC. Hogg¹, and Matthew H. England²

¹Research School of Earth Science and ARC Center of Excellence for Climate Extremes, Australian National University, Canberra, Australia

²Climate Change Research Centre (CCRC), UNSW Australia, Sydney NSW, Australia

Key Points:

- Kinetic energy of coherent eddies contain around 50% of the surface ocean kinetic energy budget.
- Seasonal cycle of the number of coherent eddies and coherent eddy amplitude reveal a 3-6 month lag to wind forcing
- Inverse cascade sets up the seasonal lag of the number and amplitude of coherent eddies.
- The coherent eddy amplitude has increase at a rate of 3 cm per decade since 1993.

15 **Abstract**

16 Ocean eddies influence regional and global climate through mixing and transport
 17 of heat and properties. One of the most recognizable and ubiquitous feature of oceanic
 18 eddies are vortices with spatial scales of tens to hundreds of kilometers, frequently re-
 19 ferred as “mesoscale eddies” or “coherent eddies”. Coherent eddies are known to trans-
 20 port properties across the ocean and to locally affect near-surface wind, cloud proper-
 21 ties and rainfall patterns. Although coherent eddies are ubiquitous, yet their climatol-
 22 ogy, seasonality and long-term temporal evolution remains poorly understood. Thus, we
 23 examine the kinetic energy contained by coherent eddies and we present the annual and
 24 long-term changes of automatically identified coherent eddies from satellite observations
 25 from 1993 to 2019. Around 50% of the kinetic energy contained by ocean eddies corre-
 26 sponds to coherent eddies. Additionally, a strong hemispherical seasonal cycle is observed,
 27 with a 3–6 months lag between the wind forcing and the response of the coherent eddy
 28 field. Furthermore, the seasonality of the number of coherent eddies and their amplitude
 29 reveals that the number of coherent eddies responds faster to the forcing (~ 3 months),
 30 than the coherent eddy amplitude (which is lagged by ~ 6 months). Our analysis high-
 31 lights the relative importance of the coherent eddy field in the ocean kinetic energy bud-
 32 get, implies a strong response of the eddy number and eddy amplitude to forcing at dif-
 33 ferent time-scales, and showcases the seasonality, and multidecadal trends of coherent
 34 eddy properties.

35 **Plain language summary**36 **1 Introduction**

37 Mesoscale ocean variability with spatial scales of tens to hundreds of kilometers is
 38 comprised of processes such as vortices, waves, and jets (Ferrari & Wunsch, 2009; Fu et
 39 al., 2010). These mesoscale processes are highly energetic, and they play a crucial role
 40 in the transport of heat, salt, momentum, and other tracers through the ocean (Wun-
 41 sch & Ferrari, 2004; Wyrtki et al., 1976; Gill et al., 1974). Possibly, the most recogniz-
 42 able and abundant process observed from satellites is mesoscale vortices. Although mesoscale
 43 vortices are commonly referred to in literature as “mesoscale eddies”, this term is also
 44 often used to describe the total mesoscale ocean variability (the time-varying component
 45 of the mesoscale flow), thus, here we will refer to mesoscale vortices as *coherent eddies*.

46 Coherent eddies are quasi-circular currents. According to their rotational direction,
47 the sea surface height anomaly within a coherent eddy can have a negative or positive
48 sea surface height anomaly (cold-core and warm-core coherent eddies, respectively). This
49 characteristic sea surface height signature of coherent eddies has been utilized to auto-
50 matically identify and track coherent eddies from satellite altimetry (Cui et al., 2020;
51 Martínez-Moreno et al., 2019; Ashkezari et al., 2016; Faghmous et al., 2015; Chelton et
52 al., 2007). Automated identification algorithms of coherent eddies have shown their ubiq-
53 uituity in the oceans, with a predominant influence at hotspots of eddy activity such as bound-
54 ary currents and the Antarctic Circumpolar Current. In these regions, Chelton et al. (2011)
55 estimated that coherent eddies contribute around 40–50% of the mesoscale kinetic en-
56 ergy (Chelton et al., 2011) and thus a significant fraction of the total kinetic energy (Fer-
57 rari & Wunsch, 2009). Although this unique estimate showcases the importance of the
58 mesoscale coherent eddy field, the energy contained by coherent eddies was estimated
59 by extracting the geostrophic velocities within the detected coherent eddies, thus it is
60 possible it may contain energy from other processes. Coherent eddies are not only abun-
61 dant and may have a large proportion of the surface kinetic energy budget, but they are
62 also essential to ocean dynamics as concluded by many previous studies (Patel et al., 2020;
63 Schubert et al., 2019; Pilo et al., 2015; Frenger et al., 2015, 2013; Beron-Vera et al., 2013;
64 Siegel et al., 2011; Hogg & Blundell, 2006).

65 There is broad consensus that mesoscale eddy kinetic energy has a pronounced sea-
66 sonal variability (Uchida et al., 2017; Kang & Curchitser, 2017; Qiu & Chen, 2004; Qiu,
67 1999). Several hypotheses have been proposed to explain this seasonality including: sea-
68 sonal variations of atmospheric forcing (Sasaki et al., 2014), seasonality of the mixed layer
69 depth (Qiu et al., 2014; Callies et al., 2015), seasonality of the intensity of barotropic in-
70 stability (Qiu & Chen, 2004), the variability of the baroclinic instability due to the sea-
71 sonality of the vertical shear (Qiu, 1999), and a seasonal lag of the inverse energy cas-
72 cade (i.e. energy is transported between scales, from small to large; Arbic et al., 2013)
73 in combination with the presence of a front in the mixed layer, which can lead to a sea-
74 sonal cycle of the baroclinic instability (Qiu et al., 2014). On one hand, processes such
75 as barotropic and baroclinic instabilities control the seasonality of coherent eddies in the
76 ocean. On the other hand, recent studies using observations and eddy-permitting climate
77 models suggest several long-term adjustments of the global ocean capable of long-term
78 changes in the coherent eddy field. Such readjustments include a multidecadal increase

in the ocean stratification resulted from temperature and salinity changes (Li et al., 2020), a horizontal readjustment of the sea surface temperature gradients (Ruela et al., 2020; Bouali et al., 2017; Cane et al., 1997), and an intensification of the kinetic energy, eddy kinetic energy, and mesoscale eddy kinetic energy over the last 3 decades as a consequence of an increase in wind forcing (Hu et al., 2020; Wunsch, 2020; Martínez-Moreno et al., 2021). All these seasonal factors and long-term readjustments directly influence the annual and decadal response of the coherent eddy field, however, the seasonality of the coherent component of the eddy kinetic energy, as well as the seasonal cycle and trends of the coherent eddy statistics remain unknown.

Here we present a new global climatology of the coherent eddy kinetic energy by reconstructing the coherent eddy signature from satellite observations. Our study documents the seasonal cycle of the coherent eddy kinetic energy, and seasonal cycle and long-term trends of the coherent eddy properties over the satellite record. Moreover, we conduct more detail analysis in regions where coherent eddies dominate the eddy kinetic energy field. This paper is structured as follows: the data sources and methodology are described in section 2. Then, we present the climatology, energy ratios, and global seasonality of the coherent eddy kinetic energy in section 3. Section 4 presents the global climatology and seasonality of coherent eddy properties, followed by long-term changes of the coherent eddy properties (section 5). Then we focus our attention on the seasonal cycle and coherent eddy properties in regions dominated by coherent eddies (section 6). Finally, section 7 summarizes the main results and discusses the implications of this study.

2 Methods

We use daily sea surface height (SSH) data made available by the Copernicus Marine Environment Monitoring Service in near real time (CMEMS, 2017). This gridded product contains the sea surface height and geostrophic velocities with daily 0.25° resolution from January 1993 to 2019. The daily geostrophic velocities allowed us to compute the kinetic energy (KE) and eddy kinetic energy (EKE) over the satellite record. The main source of EKE is the time-varying wind (Ferrari & Wunsch, 2009), thus we computed the seasonal cycle of the wind magnitude from the JRA55 reanalysis (Japan Meteorological Agency, Japan, 2013) using wind velocities at 10m above the ocean's surface.

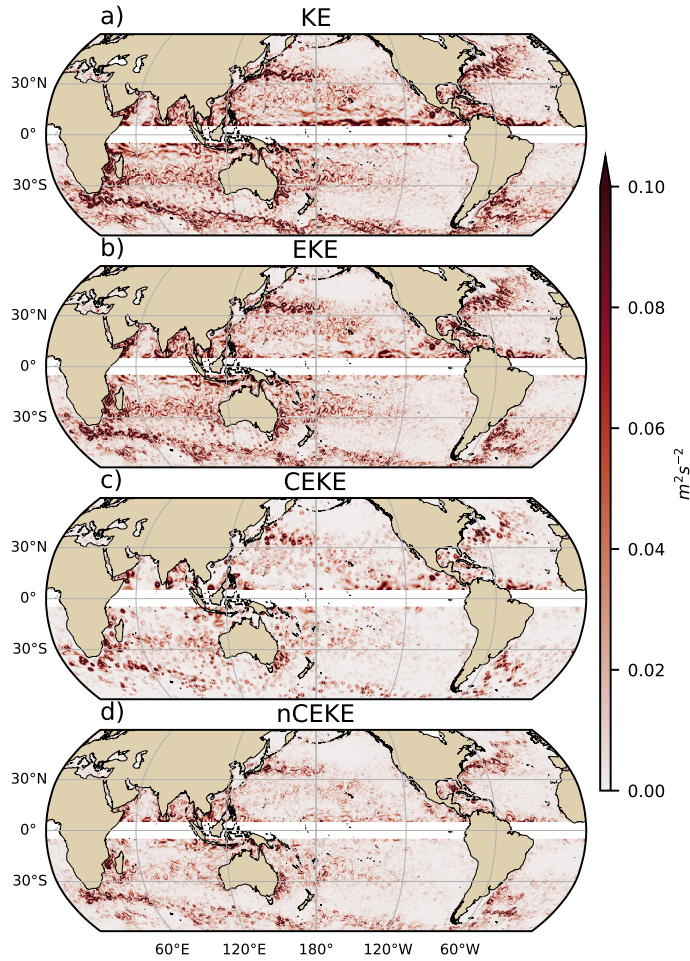
Over the same record, coherent eddy statistics from Martínez-Moreno et al. (2019), hereafter M-M, are analyzed and compared to those released by Chelton & Schlax (2013), both datasets are gridded in a 1° resolution. Although both datasets are produced via automated eddy identification algorithms using closed contours of SSH, these datasets have important differences in the criteria they use to identify and record coherent eddies statistics. The major differences include; (i) M-M's algorithm requires an adjustment between a 2D Gaussian and the SSH anomaly (SSHa) surface within the identify closed contour, while Chelton's only uses the outer-most closed contour of SSH; (ii) M-M's dataset reports the maximum SSHa within the identified coherent eddy, while Chelton's algorithm reports the maximum SSH value minus the discrete level in which the coherent eddy was identified; M-M's dataset includes all detected coherent eddies, while Chelton's dataset excludes (iii) coherent eddies with lifetimes shorter than four weeks and (iv) coherent eddy amplitudes smaller than 1cm. Moreover, M-M's algorithm allows the reconstruction of the coherent eddy field under the assumption that coherent eddies have a 2D Gaussian imprint in the sea surface height. This Gaussian reconstruction of the coherent eddy field then allow us to estimate the coherent geostrophic eddy velocities and thus the kinetic energy contained only by coherent eddies.

2.1 Kinetic Energy decomposition

Kinetic energy is commonly divided into the mean and time-varying components through a Reynolds decomposition. At a given time, the surface velocity field $\mathbf{u} = (u, v)$ is split into the time mean ($\bar{\mathbf{u}}$) and time varying components (\mathbf{u}'). Moreover, M-M proposed to further decompose the eddy kinetic energy into the energy contained by coherent features (\mathbf{u}'_e) and non-coherent features (\mathbf{u}'_n). Therefore the KE equation can be written as:

$$\text{KE} = \underbrace{\bar{u}^2 + \bar{v}^2}_{\text{MKE}} + \underbrace{u'^2_e + v'^2_e + u'^2_n + v'^2_n}_{\text{CEKE}} + \underbrace{\mathcal{O}_c^2}_{\text{nCEKE}} + \mathcal{O}^2 \quad (1)$$

Due to the properties of this decomposition, the second order term \mathcal{O}^2 is zero when averaged over the same period as $\bar{\mathbf{u}}$. However, \mathcal{O}_c^2 is not necessarily negligible, unless it is averaged over time and space. More information about the decomposition of the field into coherent features and non-coherent features is explained by Martínez-Moreno et al.



143 **Figure 1.** Snapshot of surface kinetic energy (\overline{KE}), surface eddy kinetic energy (\overline{EKE}),
 144 surface coherent eddy kinetic energy (\overline{CEKE}), and surface non-coherent eddy kinetic energy
 145 (\overline{nCEKE}) for the 1st of January 2017.

138 (2019). A global snapshot of each component of kinetic energy decomposition is shown
 139 in Figure 1, where the KE and EKE are comprised of rings and filaments. As expected,
 140 the decomposition of EKE into CEKE and nCEKE components exhibit only ring-like
 141 signatures expected of coherent eddies, while the non-coherent component shows filaments
 142 and some miss-identified coherent eddies.

146 2.2 Eddy statistics

147 The eddy statistics used in this study include (i) the eddy count ($cEddy_n$) defined
 148 as the number of eddies per grid cell, (ii) the eddy diameter defined as the diameter of

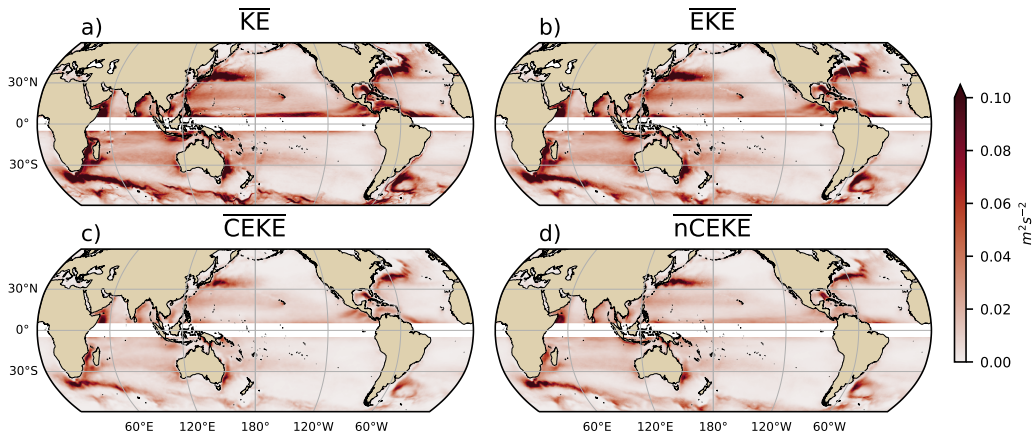
a circle with equal area as the closed contour of the identified eddy, and (iii) the mean eddy amplitude defined as the mean amplitude of the coherent eddies within the cell ($cEddy_{amp}$). The latter metric can be separated into positive ($cEddy_{amp}^+$) and negative ($cEddy_{amp}^-$) coherent eddy amplitudes, defined as the mean amplitude of warm core and cold core coherent eddies, respectively, within the cell. The absolute eddy amplitude ($|cEddy_{amp}|$) is then defined as:

$$|cEddy_{amp}| = \frac{1}{2} (cEddy_{amp}^+ - cEddy_{amp}^-) \quad (2)$$

Note that the $cEddy_{amp}^+$ and $cEddy_{amp}^-$ are sign definite, thus the difference will always be positive, mean $cEddy_{amp}$ can be negative or positive noting the dominant polarity of coherent eddies in the region. We analyze the climatology, seasonal cycles and trends of the eddy statistics between 1993 and 2019. We exclude the equatorial region (10°S - 10°N) and poleward of 60° . Note that the climatology of $cEddy_n$ is computed by adding all the identified eddies over the record, while all other climatological statistics are computed as the time-average over the record. Seasonal climatologies are calculated for the monthly average of each coherent eddy statistic, while hemispherical time-series are filtered with a running average of 90 days. Trends of $cEddy_n$ and $|cEddy_{amp}|$ are calculated by coarsening the dataset to a 5° grid, and then linear trends are computed for each grid point, the statistical significance is assessed by a modified Mann-Kendall test (Yue & Wang, 2004). Time averages are denoted by $\overline{}$, while area averages are shown by $\langle \rangle$.

3 Global Coherent Eddy Energetics

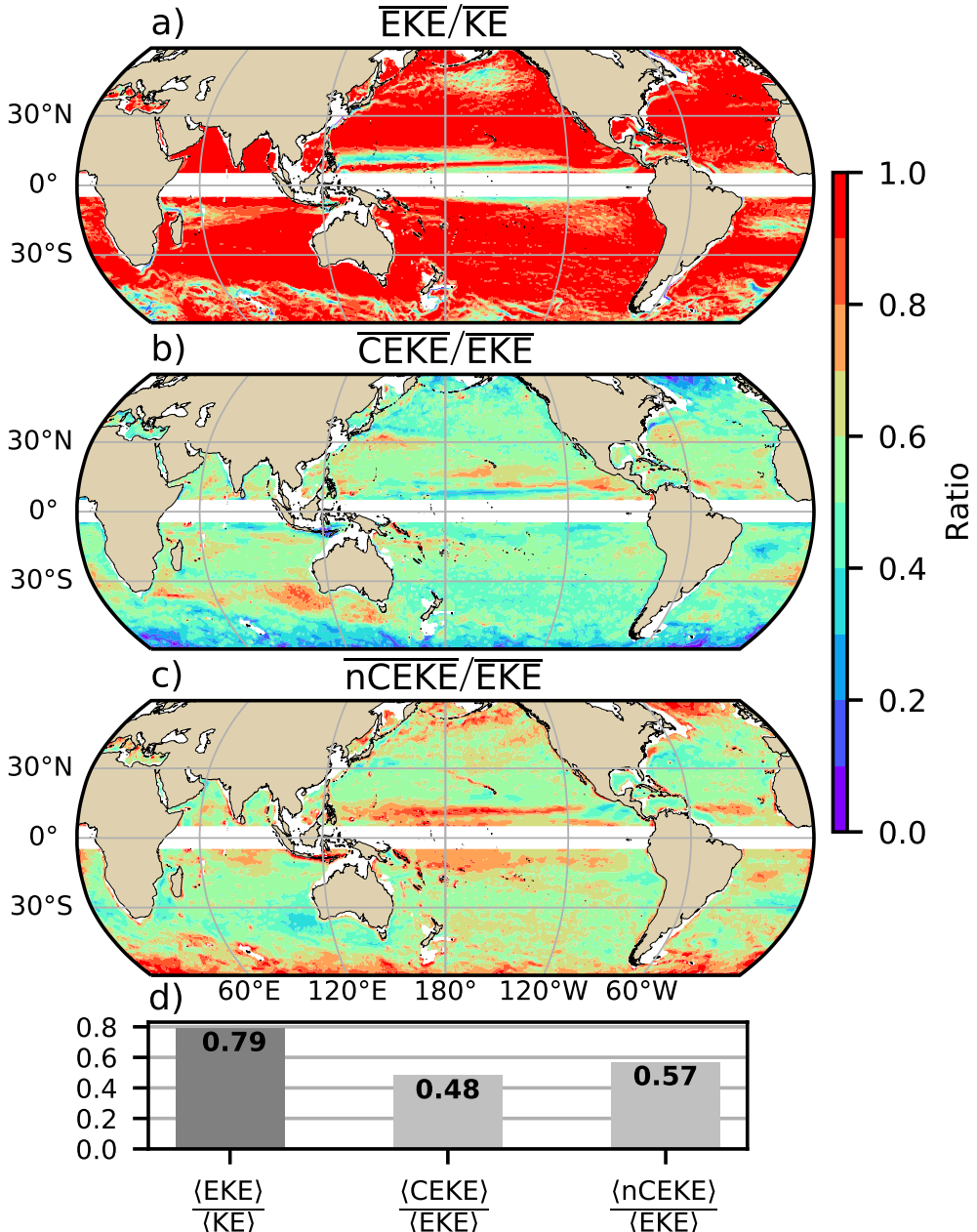
The climatology of the kinetic energy decomposition estimated from sea surface height is shown in Figure 2. These maps show that many regions of the global ocean are highly energetic in mean KE (\overline{KE}), mean EKE (\overline{EKE}), mean coherent eddy kinetic energy (\overline{CEKE}) and mean non-coherent eddy kinetic energy (\overline{nCEKE}). The spatial pattern highlights well known regions of the ocean, where mesoscale processes are abundant, such is the case of western boundary currents, the Antarctic Circumpolar Current and regions within the ocean gyres. Remarkably, the spatial distribution of the energy contained by the reconstructed mesoscale coherent eddies and non-coherent components are similar (Figures 2c,d). This can be thought as regions where mesoscale activity is intense, however, there are some regions where coherent eddies dominate over non-coherent and vice-versa. Overall, this decomposition suggest that boundary currents and other energetic regions,



181 **Figure 2.** Climatology of surface kinetic energy (\overline{KE}), surface eddy kinetic energy (\overline{EKE}),
182 surface coherent eddy kinetic energy (\overline{CEKE}), and surface non-coherent eddy kinetic energy
183 (\overline{nCEKE}) between 1993-2018.

179 in particularly, eddy-rich regions in the ocean contain both coherent and non-coherent
180 components of the kinetic energy.

193 Eddy kinetic energy is known to be more than an order of magnitude greater than
194 MKE (Gill et al., 1974), this is clearly shown in Figure 3a, where the ratio of \overline{EKE} is re-
195 sponsible of almost all the \overline{KE} across the ocean, except for regions with persistent cur-
196 rents over time. Such regions are located in the mean boundary current locations, the
197 equatorial pacific currents and regions in the Antarctic Circumpolar current, where the
198 EKE explains around 40% of the \overline{KE} . As estimated by a previous study by Chelton et
199 al. (2011), the EKE within coherent eddies with lifetimes greater than 4 weeks contain
200 between 40 to 60 percent of the \overline{EKE} . Our result from reconstructing the coherent eddy
201 signature (Figure 3b) further corroborates that the coherent component (\overline{CEKE}) has around
202 $\sim 48\%$ of the \overline{KE} (Figure 3d). Furthermore, global area averages of the ratios show \overline{EKE}
203 explains approximately $\sim 78\%$ of the ocean \overline{KE} field, while non coherent eddy features
204 contain $\sim 57\%$ percent of the \overline{EKE} . Note the globally averaged coherent and non coher-
205 ent components do not add to 100% as the cross terms (O_c^2) are different to zero, as re-
206 gions with negligible EKE are double counted in the CEKE and nCEKE ratios, and co-
207 herent eddy reconstruction errors. The spatial pattern reveals a dominance of the \overline{CEKE}
208 equatorward from the boundary currents and areas with large coherent eddy contribu-
209 tions of around 80% of the region's eddy kinetic energy can be found south of Australia,



184 **Figure 3.** Ratios of the kinetic energy components. a) Map of the proportion of mean eddy
 185 kinetic energy (EKE) versus mean kinetic energy (\bar{KE}); b) Map of the percentage of mean co-
 186 herent eddy kinetic energy (\bar{CEKE}) versus mean eddy kinetic energy (\bar{EKE}); c) Map of the
 187 percentage of mean non-coherent eddy kinetic energy (\bar{nCEKE}) versus mean eddy kinetic en-
 188 ergy (\bar{EKE}); d) Global area averaged percentage of mean eddy kinetic energy ($\langle EKE \rangle$) versus
 189 the global mean kinetic energy ($\langle \bar{KE} \rangle$), area averaged percentage of mean coherent eddy kinetic
 190 energy ($\langle \bar{CEKE} \rangle$) and mean non coherent eddy kinetic energy ($\langle \bar{nCEKE} \rangle$) versus global mean
 191 eddy kinetic energy ($\langle \bar{EKE} \rangle$). Regions where the depth of the ocean is shallower than 1000m are
 192 removed from the ratio estimation.

210 the Tehuantepec Gulf, and the South Atlantic. An evident signal is an reduction of the
 211 energy contained by coherent eddies at high latitudes and an increase in the energy ex-
 212 plained by non-coherent eddies, this could be a consequence of the incapability of the
 213 0.25° satellite resolution (~ 13 km at 60°) to resolve coherent eddies with scales smaller
 214 than ~ 10 km (first baroclinic Rossby radius at 60°).

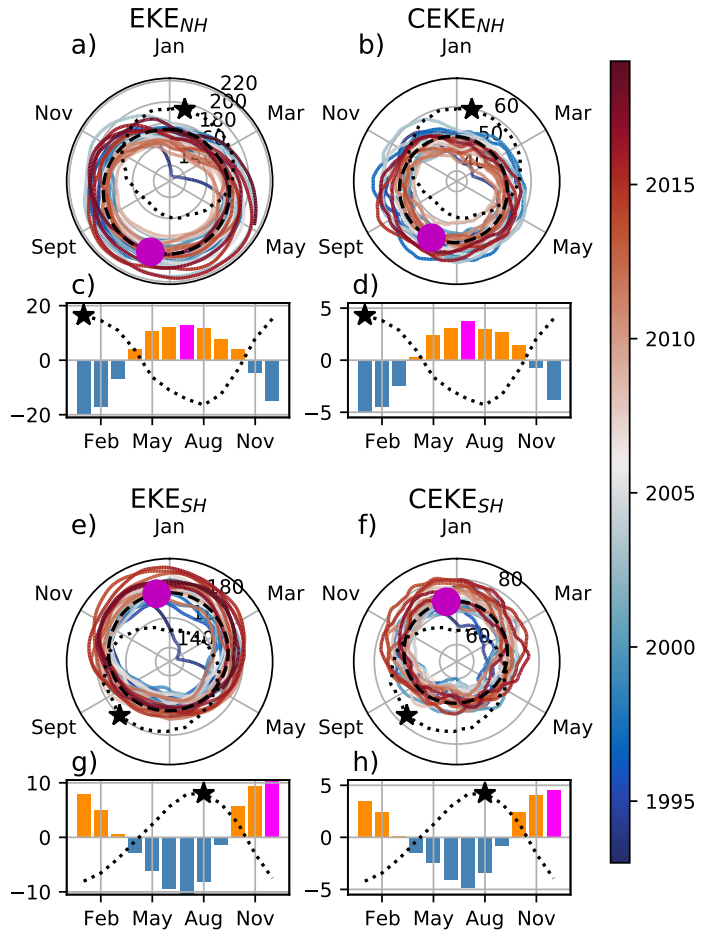
215 **3.1 Seasonality**

216 Figure 4 shows the seasonal cycle of the EKE and CEKE for the northern hemi-
 217 sphere (NH; 10°N - 60°N) and Southern Hemisphere (SH; 60°S - 10°S). In both hemi-
 218 spheres, the EKE and CEKE peak during the hemispherical summer. In the northern
 219 hemisphere, the largest EKE and CEKE occurs ~ 6 months after the maximum winds
 220 (Figure 4c and d), while the Southern ocean seems to respond within ~ 4 months (Fig-
 221 ure 4g, and h). This seasonal lag and maximum is consistent with a time-lag of the in-
 222 verse cascade (Sasaki et al., 2014; Qiu et al., 2014) where winter has the highest energy
 223 at the smallest scales (non-solvable with satellite observations), spring and autumn have
 224 the highest and lowest energy in scales of 50-100 km, and summertime has the highest
 225 energy at the largest scales (> 100 km; Uchida et al. 2017), thus the maximum of EKE
 226 and CEKE located during summertime suggest the seasonality of eddies and coherent
 227 eddies could be dominated by scales larger than 100 km.

228 The cyclic plots in Figure 4 shows the temporal evolution of EKE and CEKE. Note
 229 that high frequency variability can be observed in the CEKE field with temporal scales
 230 of a few months, this could be attributed local dynamics averaged over the hemisphere,
 231 as well as errors within the coherent eddy reconstruction. Additionally, cyclic plots high-
 232 light long-term temporal changes over the record; (i) northern hemisphere winters show
 233 a decrease in the CEKE field and (ii) the Southern hemisphere show concentric growth
 234 over time in EKE and CEKE, which support the increasing trends in the Southern Ocean
 235 observed by Hogg et al. (2015), Martínez-Moreno et al. (2019), and Martínez-Moreno
 236 et al. (2021).

243 **4 Global Coherent Eddy Statistics**

244 Automated algorithms allows to estimate the contribution and temporal changes
 245 of eddy properties, in particular, their abundance as the number of eddies and their in-



237 **Figure 4.** Hemispherical seasonality of eddy kinetic energy (EKE), coherent eddy kinetic en-
 238 ergy (CEKE). Panels a, and b show the northern hemisphere seasonal cycle, while panels c, and
 239 d correspond to the southern hemisphere. Dashed lines correspond to the seasonal cycle of the
 240 fields and dotted lines show the seasonal cycle of the wind magnitude smoothed over 120 days
 241 (moving average). The green and magenta stars show the maximum of the seasonal cycle for the
 242 kinetic energy components and the wind magnitude, respectively. The line colors show the year.

tensity, namely their amplitude and diameter. Figure 5 shows gridded climatologies of the number of eddies and the eddy amplitude. We compare M-M eddy count against Chelton et al. (2007) (Figure 5a-b). Although the number of the identified eddies is larger in M-M, possibly due to the lifespan filter implemented by Chelton, both datasets reveal consistent spatial patterns. For example, both datasets show high abundance of eddies in the East North Pacific, East North Atlantic, as well as the East South Pacific, East South Atlantic and East Indian Ocean, and small number counts of eddies in the tropics and in high latitudes ($\sim 60^\circ$). An interesting pattern also emerges in both eddy count datasets, where clusters with larger eddy counts are favored across the ocean, in addition, coherent eddy propagation patterns can be observed in boundary currents and regions in the Southern Ocean. These clusters and paths of coherent eddies could be associated with topographic features, however it remains puzzling the consistency of the eddy count pattern.

Regions with large counts of eddies have in general small absolute amplitudes (Figure 5 c), ocean gyre interiors follow with a larger absolute amplitude and finally regions such as the boundary currents and Antarctic Circumpolar Current have the largest coherent eddy absolute amplitudes as shown by Chelton et al. (2011). Eddy amplitude highlights regions dominated by a given coherent eddy polarity, for example, boundary currents have a preferred sign (Figure 5 d); positive amplitude polewards of the boundary current mean location, and negative amplitude equatorwards. This sign preference is consistent with the way coherent eddies are shed from boundary currents. These global statistics reveal the absolute coherent eddy amplitude is a proxy of the CEKE with similar spatial patterns (Figure 2 & Figure 5 c) and showcases that regions where $\overline{\text{CEKE}}$ has a large proportion of $\overline{\text{EKE}}$ (Figure 3), the absolute coherent eddy amplitude is also important.

276 4.1 Seasonality

To further understand the seasonal cycle of CEKE, we compute hemispherical seasonality of the coherent eddy properties (Figure 6). The seasonality of the number of eddies in the Northern Hemisphere peaks on April (Figure 6 a, c), while the Southern Hemisphere maximum number of eddies occurs during October (Figure 6 e, g). Meanwhile, the seasonality of the absolute eddy amplitude peaks in August and January for the Northern and Southern Hemispheres respectively (Figure 6 b, d, f, and h). As expected, the

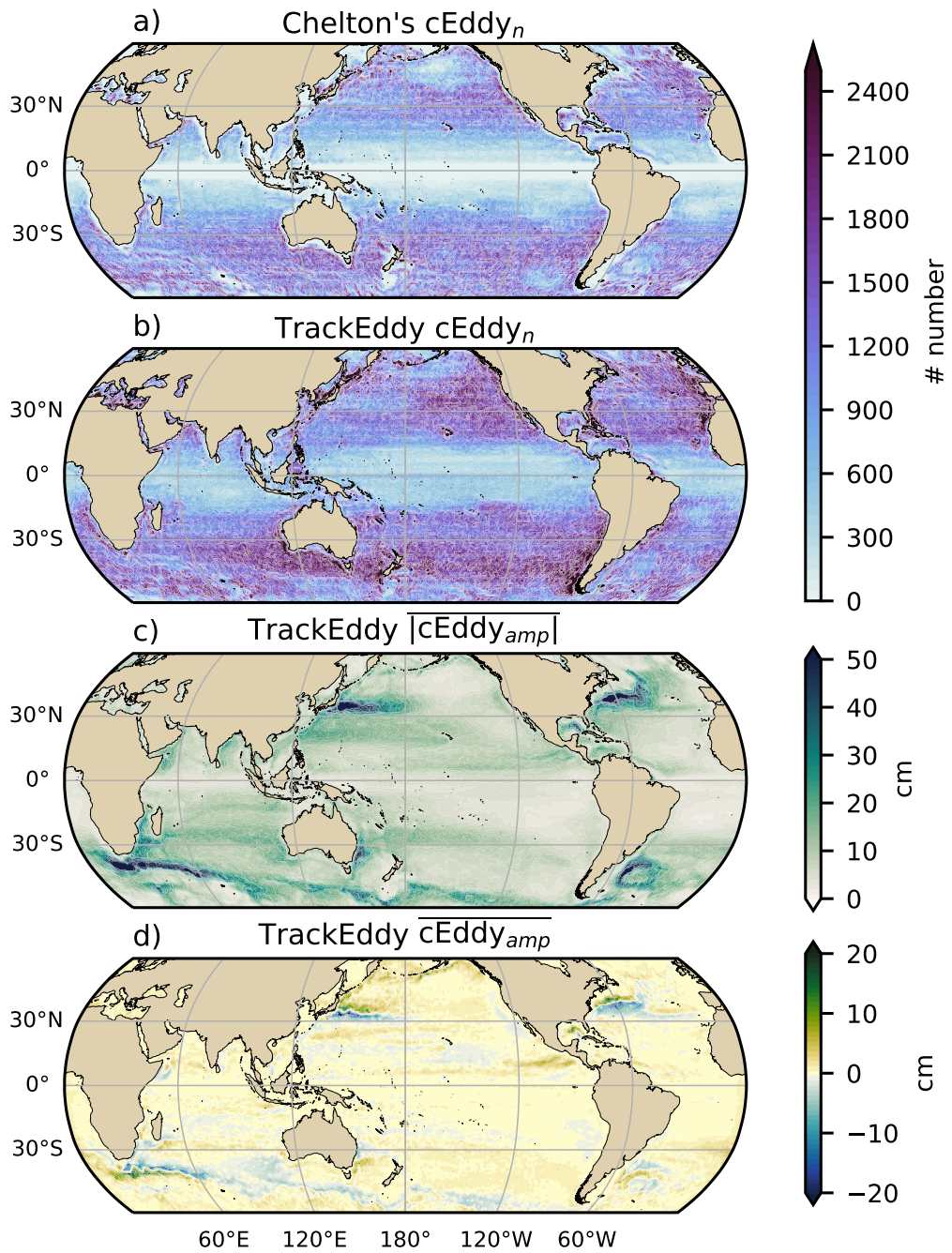
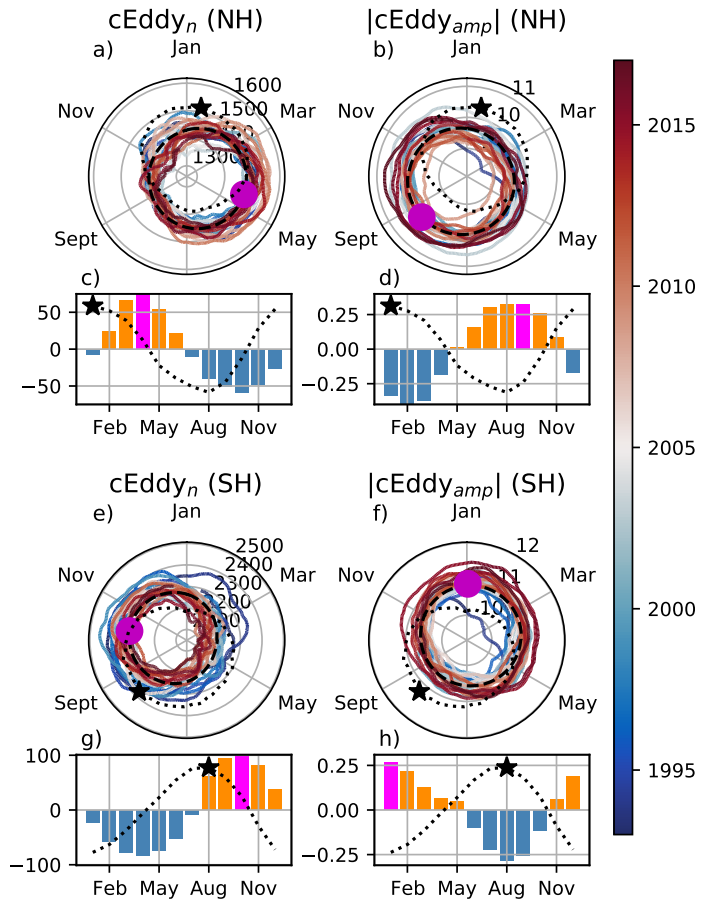


Figure 5. Climatology of the coherent eddy statistics. a) Climatology of the number of coherent eddies ($cEddy_n$) identified by Chelton et al. (2007); b) Climatology of the number of coherent eddies ($cEddy_n$) identified by Martínez-Moreno et al. (2019); c) Climatology of the mean absolute coherent eddy amplitude ($cEddy_{amp}$). d) Climatology of the mean coherent eddy amplitude ($cEddy_{amp}$).

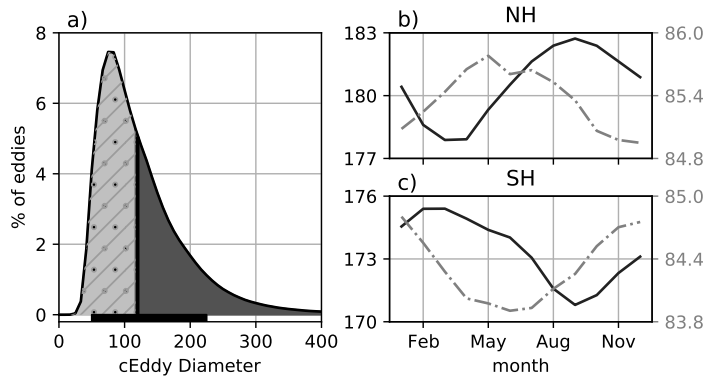
283 seasonality of the absolute eddy amplitude or intensity of the coherent eddies is consis-
284 tent with the seasonal cycle of CEKE. Furthermore, a distinct lag of \sim 3 months is ob-
285 served between the winds and eddy count, while the eddy amplitude maximum occurs
286 \sim 6 months after the seasonal maxima in winds. This lag suggest the eddy number in-
287 creases earlier in the year and through eddy-eddy interactions (merging of coherent ed-
288 dies) the amplitude of the coherent eddy increases. This can be further explored by look-
289 ing at the eddy diameter. Note that 90% of identified eddies have diameters between 50
290 to 220 km (Figure 7 a), but more importantly, we observe in the Northern Hemisphere
291 large-scale coherent eddies (diameter > 120 km) maximum diameter occur during Septem-
292 ber, while small-scale coherent eddies (diameter < 120 km) seasonal peak is during May
293 (Figure 7 b). Meanwhile, in the Southern Hemisphere, the large-scale coherent eddies
294 occurs in February, while the small-scale coherent eddies peak in December (Figure 7 c).
295 This result is consistent with baroclinic instabilities generating many small coherent ed-
296 dies early, which then are capable to merge and grow to become larger and more ener-
297 getic. This process can be thought analogous to the inverse energy cascade, thus this mech-
298 anism not only drives the EKE seasonality, but also may be responsible of the seasonal
299 cycle of coherent eddies.

300 Long-term changes can be observed in Figure 6a,b, e, and f where growing-shrinking
301 concentric circles over time denote an increase-decrease trend of the field. This is par-
302 ticularly evident in the Southern Hemisphere, where the number of eddies has decreased,
303 the eddy amplitude has increased. This result is consistent with the observed trends in
304 EKE and mesoscale EKE in the Southern Ocean (Hogg et al., 2015; Martínez-Moreno
305 et al., 2021). Furthermore, by analogy we extend the argument that a long-term decrease
306 in the number of coherent eddies and increase in coherent eddy amplitude could be a con-
307 sequence of a long-term increase in the energy cascade, where interactions between ed-
308 dies may become more frequent and result in stronger coherent eddies. This hypothe-
309 sis may also occur in conjunction with other processes, such as baroclinic and barotropic
310 instabilities generating stronger eddies.

326 The coherent eddy amplitude from positive coherent eddies and negative coherent
327 eddies show similar seasonal cycles to the absolute eddy amplitude (Figure 8). However,
328 by separating the polarity contribution, its observed that the amplitude of negative co-
329 herent eddies in the Northern Hemisphere has decreased (Figure 8b). In the Southern



311 **Figure 6.** Hemispherical seasonality of the coherent eddy statistics; a,e) seasonal cycle of the
 312 number of coherent eddies ($cEddy_n$); b,f) seasonal cycle of the mean coherent eddy amplitude
 313 ($cEddy_{amp}$); c,g) seasonal cycle of the warm core coherent eddies amplitude (positive $cEddy_{amp}$);
 314 d,h) seasonal cycle of the cold core coherent eddies amplitude (negative $cEddy_{amp}$). Panels a,b
 315 and c show the northern hemisphere seasonal cycle, while panels d,e, and f correspond to the
 316 southern hemisphere. Dashed lines correspond to the seasonal cycle of the fields and dotted lines
 317 show the seasonal cycle of the wind magnitude smoothed over 120 days (moving average). The
 318 green and magenta stars show the maximum of the seasonal cycle for each field and the wind
 319 magnitude, respectively. The line colors show the year.

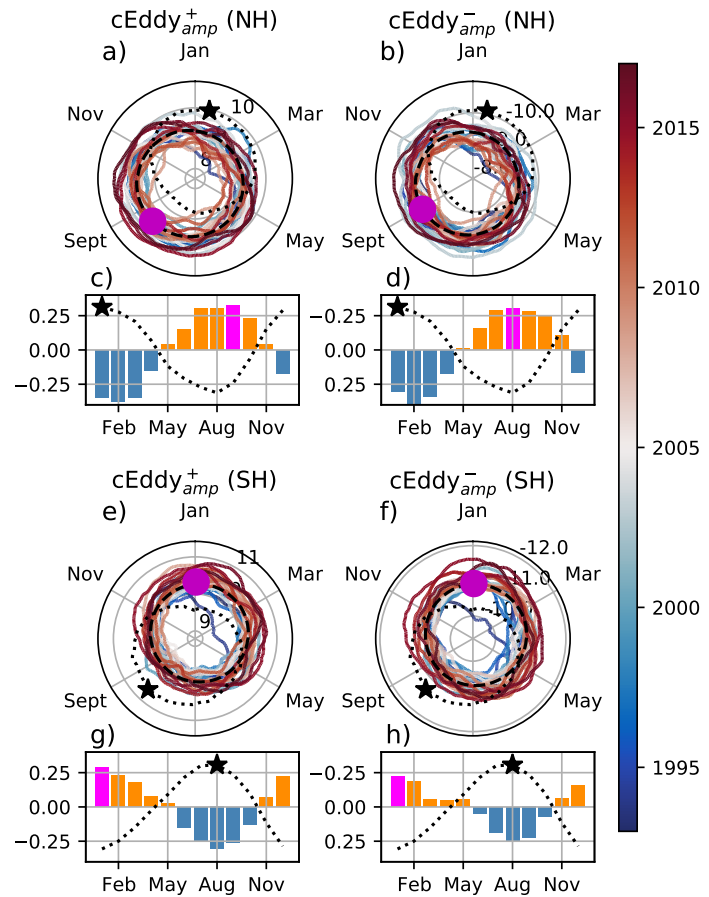


320 **Figure 7.** Distribution of the identified eddy diameter and hemispherical seasonality of the
 321 coherent eddy diameter. a) Distribution in percentage of identified eddy amplitude, solid bar bel-
 322 low distribution represents 90% of the identified eddies. Seasonal cycle of the eddy diameter for
 323 the b) Northern Hemisphere and c) Southern Hemisphere. Dark solid line and area corresponds
 324 to coherent eddies with diameters larger than 120 km, while light gray dash-dotted line and area
 325 shows coherent eddies with diameters smaller than 120 km.

330 Ocean, the increase in absolute eddy amplitude is further corroborated as both coher-
 331 ent eddy polarities show an increase since the early 90s (Figure 8e,f).

341 5 Trends

342 It is expected from the results presented in Figures 4, 6, and 8 a long-term read-
 343 justment of the coherent eddy field. The long-term trends of the number of coherent ed-
 344 dies, absolute coherent eddy amplitude, and coherent eddy amplitude polarities are ex-
 345 plored in Figure 9. Chelton's and M-M datasets show consistent spatial patterns in the
 346 trends and significance of the number of coherent eddies and the absolute coherent eddy
 347 amplitude. Several regions in the ocean, such as the Southern Ocean, North Atlantic and
 348 North Pacific show a decrease in the number of eddies, meanwhile those same regions
 349 have a clear increase in the absolute coherent eddy amplitude. This collocation of de-
 350 crease in number and increase in eddy amplitude provides more evidence of a possible
 351 intensification of the coherent eddy field through eddy-eddy interactions. These trends
 352 are similar to those observed in mesoscale eddy kinetic energy (Martínez-Moreno et al.,
 353 2021) and provide additional evidence of a readjustment of the mesoscale eddy field over
 354 the last 3 decades.



332 **Figure 8.** Hemispherical seasonality of the coherent eddy statistics; a,e) seasonal cycle of the
 333 number of coherent eddies ($c\text{Eddy}_n$); b,f) seasonal cycle of the mean coherent eddy amplitude
 334 ($c\text{Eddy}_{amp}$); c,g) seasonal cycle of the warm core coherent eddies amplitude (positive $c\text{Eddy}_{amp}$);
 335 d,h) seasonal cycle of the cold core coherent eddies amplitude (negative $c\text{Eddy}_{amp}$). Panels a,b
 336 and c show the northern hemisphere seasonal cycle, while panels d,e, and f correspond to the
 337 southern hemisphere. Dashed lines correspond to the seasonal cycle of the fields and dotted lines
 338 show the seasonal cycle of the wind magnitude smoothed over 120 days (moving average). The
 339 green and magenta stars show the maximum of the seasonal cycle for each field and the wind
 340 magnitude, respectively. The line colors show the year.

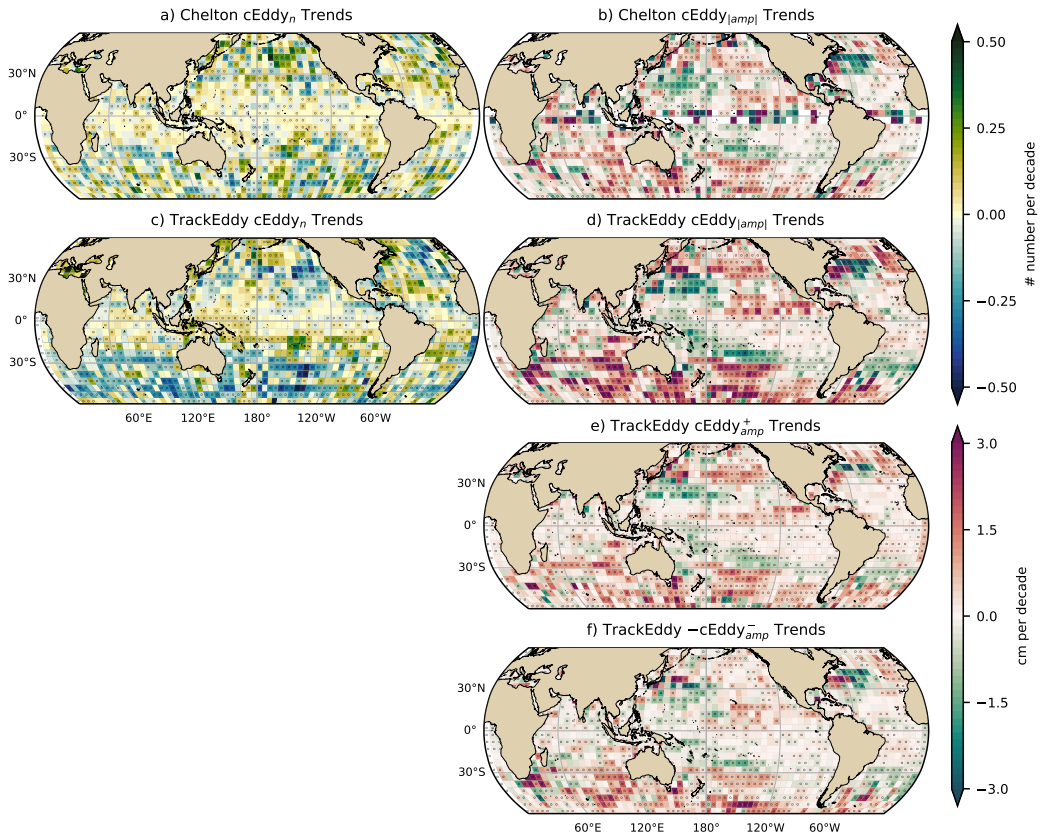
355 Although the observed trends in $|cEddy_{amp}|$ ($\sim 3\text{cm}$) have the same scale as sea level
 356 rise ($\sim 3\text{cm}$) by analyzing the positive and negative coherent eddy amplitude we can dis-
 357 card the observed trends correspond to an increase in sea level. In fact, each coherent
 358 eddy polarity has intensified in the Southern Ocean and North East Pacific and Atlantic.
 359 In other words, the absolute amplitude of each polarity has increased over time, thus this
 360 strengthening is an intrinsic response of the coherent eddy field. Note that the negative
 361 coherent eddy amplitude dominates the global $|cEddy_{amp}|$ trends (Figure 9e, f). How-
 362 ever, different trend pattern can be observed in both positive and negative coherent eddy
 363 amplitudes in the north Atlantic and north Pacific, where the negative coherent eddy
 364 amplitude in the Western Boundary Currents appears to decrease and is consistent with
 365 Figure 8.

373 6 Regional

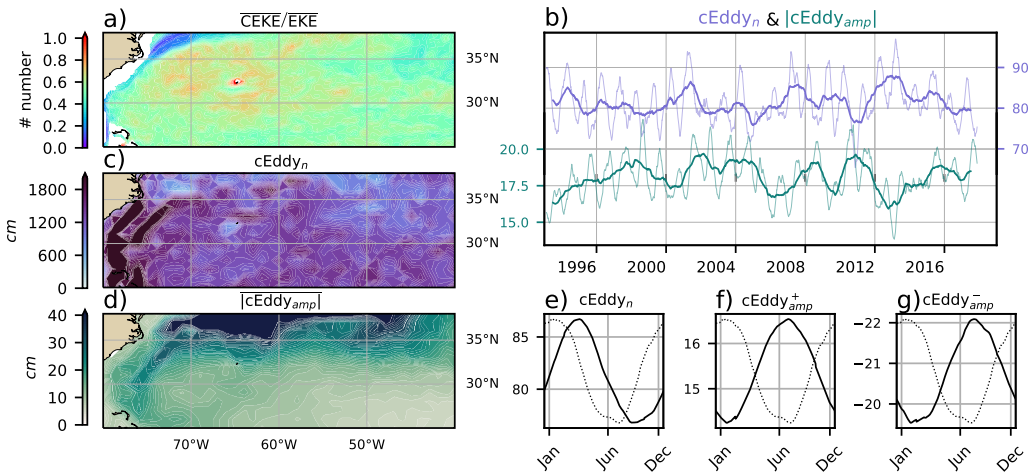
374 For regions with relatively large proportions of CEKE located at boundary currents
 375 and eastern currents, we investigate the seasonal and long-term variability of the coher-
 376 ent eddy properties.

377 The most energetic western boundary currents include; the Gulf Stream, the Kuroshio
 378 Current, and the Agulhas Current (Figures 10, 11, and 12). Coherent eddy generation
 379 in boundary currents occurs through baroclinic and barotropic instabilities of the mean
 380 current, thus all these currents share similar generation dynamics. In all these currents
 381 without exception; (i) CEKE contains around 80% of the EKE in regions equatorwards
 382 from the mean western boundary current location, (ii) the number of eddies is consis-
 383 tently larger equatorwards from the mean western boundary current location, and (iii)
 384 the absolute eddy amplitude is larger polewards of the mean western boundary current
 385 location.

386 In the Gulf Stream, the energy ratio between CEKE and EKE is $\sim 55\%$ (Figure 10).
 387 The highest energy content occurs in regions with numerous eddies, but it follows closer
 388 by regions where the largest $|cEddy_{amp}|$ gradients occurs. The time series of $cEddy_n$ and
 389 $|cEddy_{amp}|$ are anti-correlated (-0.52), and they display inter-annual and seasonal vari-
 390 ability. Although Chaudhuri et al. (2009) observed a positive phase of North Atlantic
 391 Oscillation (NAO) exhibit higher EKE, due to an increase in baroclinic instabilities, thus
 392 suggesting more coherent eddies, we do not find a correlation between the $cEddy_n$ or the



366 **Figure 9.** Trends of coherent eddy statistics. a) and b) Trends of the number of identified
 367 coherent eddies from satellite observations identified using TrackEddy, and those reported in
 368 Chelton's dataset. c) and d) Trends of the mean absolute value of identified coherent eddies am-
 369 plitude from satellite observations identified using TrackEddy, and those reported in Chelton's
 370 dataset. e) and f) Trends of eddy amplitude polarity using TrackEddy. Gray stippling shows
 371 regions that are statistically significant above the 95% confidence level. **Change cEddy_{|amp|} to**
 372 **|cEddy_amp|**

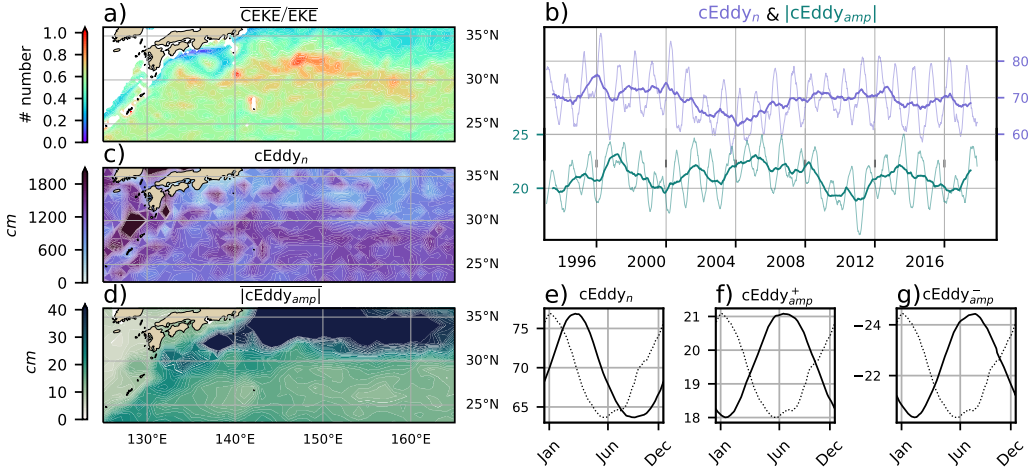


396 **Figure 10.** Climatology of the eddy field and coherent eddy field at the Gulf Stream. a) Ratio
 397 of mean coherent eddy kinetic energy ($\overline{\text{CEKE}}$) versus mean eddy kinetic energy ($\overline{\text{EKE}}$); b) Thick
 398 lines show the running average over 2 years and thin lines show the running average over 90 days
 399 of the coherent eddy number sum and the average absolute coherent eddy amplitude; c) Map of
 400 the number of eddies; d) Map of the average absolute coherent eddy amplitude; e) Seasonal cycle
 401 of the number of eddies f) Seasonal cycle of the positive coherent eddy amplitude. g) Seasonal
 402 cycle of the negative coherent eddy amplitude.

393 $|\text{cEddy}_{amp}|$ in the Gulf Stream and the NAO. Similar to the signal observed in the hemi-
 394 spherical analysis, the eddy count seasonal cycle follows the wind maximum after ~ 3 months,
 395 while the amplitude of the coherent eddies lags by ~ 6 months.

403 The variability of the cEddy_n and $|\text{cEddy}_{amp}|$ in the Kuroshio Current are weakly
 404 anti-correlated (-0.4; Figure 11). However, on average 56% of the energy in the region
 405 corresponds to CEKE. As observed in the Gulf Stream, there is an important seasonal
 406 cycle in the boundary currents, where the eddy count seasonal cycle occurs on March
 407 after ~ 3 months of the wind maximum (January). Meanwhile, the amplitude of the co-
 408 herent eddies lags by ~ 6 months (June) after the maximum wind.

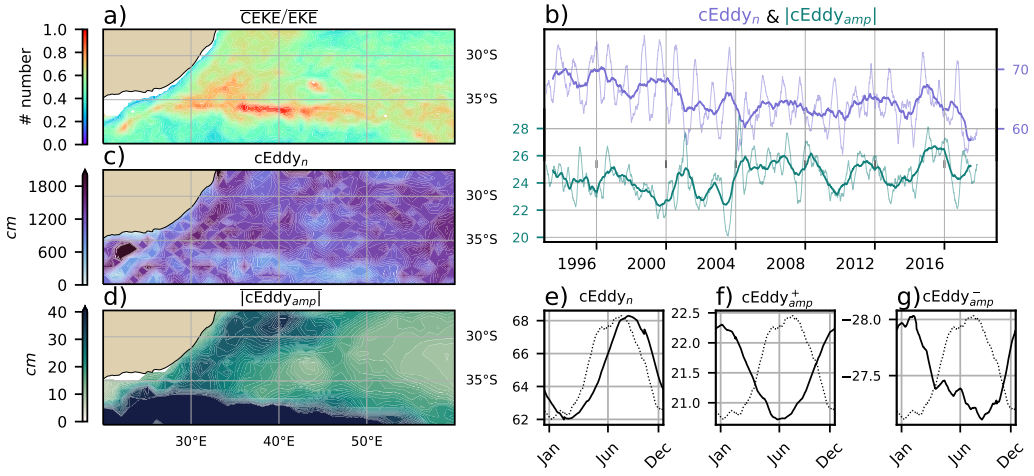
415 In the Southern Ocean, the strongest boundary current, the Agulhas Current show
 416 similar behavior than its counterparts in the Northern hemisphere (Figure 12). On av-
 417 erage, coherent eddies in the Agulhas current contain $\sim 56\%$ of the energy, meanwhile
 418 the cEddy_n seasonal peak occurs in August, while the $|\text{cEddy}_{amp}|$ occurs in January-



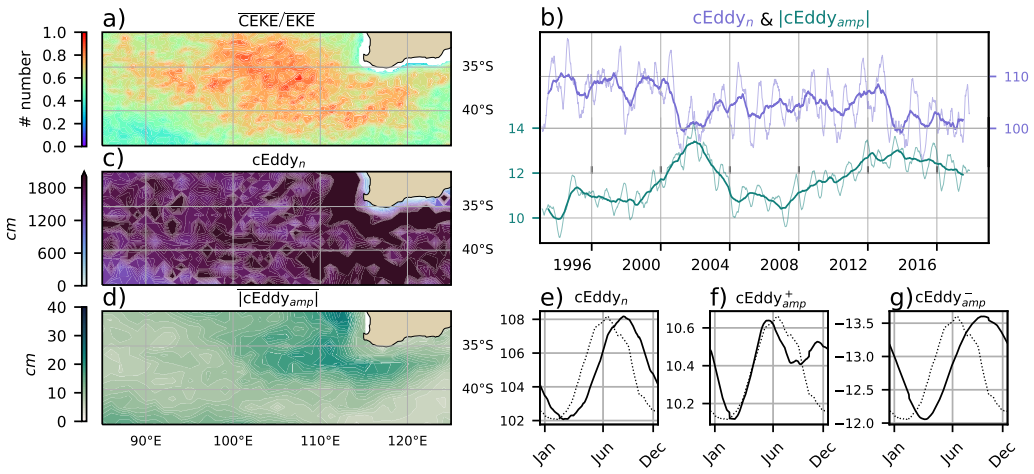
409 **Figure 11.** Climatology of the eddy field and coherent eddy field at the Kuroshio Current. a)
 410 Ratio of mean coherent eddy kinetic energy ($\overline{\text{CEKE}}$) versus mean eddy kinetic energy ($\overline{\text{EKE}}$); b)
 411 Time-series of the coherent eddy number and the average absolute coherent eddy amplitude; c)
 412 Map of the number of eddies; d) Map of the average absolute coherent eddy amplitude; Seasonal
 413 cycle of the e) number of eddies, f) positive coherent eddy amplitude, and g) negative coherent
 414 eddy amplitude. Different lines represent the same as in Figure 10.

419 February. The seasonal lag between the eddy count, eddy amplitude, and winds in west-
 420 ern boundary currents is interpreted as being analogous to the explanation presented in
 421 section 4.1 of the lagged response of coherent eddy properties due to eddy-eddy inter-
 422 actions and the inverse cascade of energy.

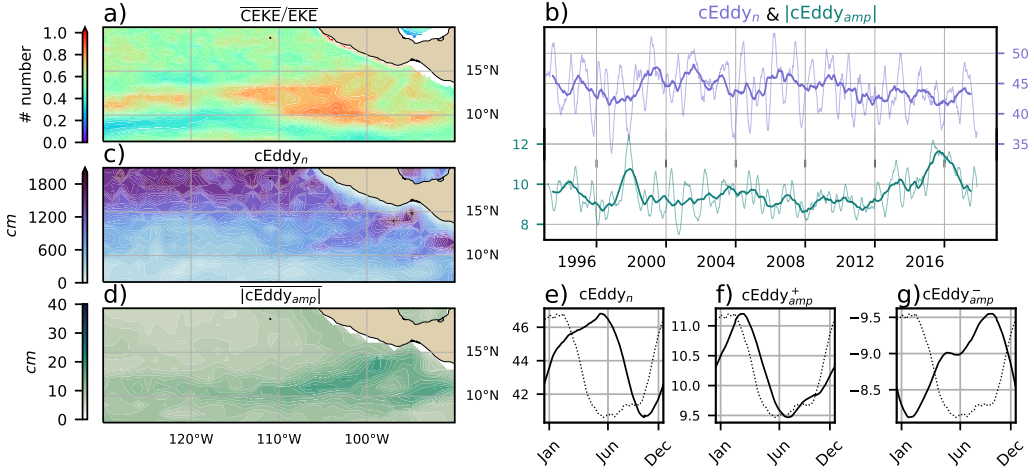
429 Note that coherent eddies dominate the EKE field in other regions such as the Leeuwin
 430 Current (Figure 13), where the 65% of the energy is contained by coherent eddies. Al-
 431 though the Leeuwin region is not characterized by having a large EKE, a considerable
 432 amount of eddies is observable across the region, but more importantly the coherent eddy
 433 amplitude is particularly large in those regions where coherent eddies dominate. The
 434 series reveal a significant increase in the $|\text{cEddy}_{amp}|$, while the cEddy_n has decreased over
 435 the last 3 decades. The seasonal cycle shows that the cEddy_n peak occurs on August,
 436 3 months after the maximum winds (June). Meanwhile, the cEddy_{amp}^+ responds in syn-
 437 chrony to winds, and the cEddy_{amp}^- is in phase with the seasonal cycle of the cEddy_n .



423 **Figure 12.** Climatology of the eddy field and coherent eddy field at the Agulhas Current. a)
424 Ratio of mean coherent eddy kinetic energy ($\overline{\text{CEKE}}$) versus mean eddy kinetic energy ($\overline{\text{EKE}}$); b)
425 Time-series of the coherent eddy number and the average absolute coherent eddy amplitude; c)
426 Map of the number of eddies; d) Map of the average absolute coherent eddy amplitude; Seasonal
427 cycle of the e) number of eddies, f) positive coherent eddy amplitude, and g) negative coherent
428 eddy amplitude. Different lines represent the same as in Figure 10.



438 **Figure 13.** Climatology of the eddy field and coherent eddy field at the Leeuwin Current. a)
439 Ratio of mean coherent eddy kinetic energy ($\overline{\text{CEKE}}$) versus mean eddy kinetic energy ($\overline{\text{EKE}}$); b)
440 Time-series of the coherent eddy number and the average absolute coherent eddy amplitude; c)
441 Map of the number of eddies; d) Map of the average absolute coherent eddy amplitude; Seasonal
442 cycle of the e) number of eddies, f) positive coherent eddy amplitude, and g) negative coherent
443 eddy amplitude. Different lines represent the same as in Figure 10.



456 **Figure 14.** Climatology of the eddy field and coherent eddy field at the East Tropical Pacific.
 457 a) Ratio of mean coherent eddy kinetic energy ($\overline{\text{CEKE}}$) versus mean eddy kinetic energy ($\overline{\text{EKE}}$);
 458 b) Time-series of the coherent eddy number and the average absolute coherent eddy amplitude;
 459 c) Map of the number of eddies; d) Map of the average absolute coherent eddy amplitude; Sea-
 460 sonal cycle of the e) number of eddies, f) positive coherent eddy amplitude, and g) negative
 461 coherent eddy amplitude. Different lines represent the same as in Figure 10.

444 Another region with important contributions of the coherent eddy field is the East
 445 Tropical Pacific (Tehuantepec region; Figure 14), where coherent eddies contain $\sim 58\%$
 446 of the energy. In fact, coherent eddy generation in this region is modulated by winds and
 447 coast trapped waves which produce a strong horizontal and vertical shear (baroclinic and
 448 barotropic instabilities; Zamudio et al., 2006). Furthermore, the equatorial generated waves
 449 propagating along the coast have an important interannual variability observable in the
 450 $|\text{cEddy}_{amp}|$ time-series, where El Niño events are notable during 1997 and 2015 (Figure
 451 14b). The seasonal cycle of cEddy_n , cEddy_{amp}^+ , and cEddy_{amp}^- supports the idea of a
 452 coherent eddies responding to two different coherent eddy generation mechanisms; the
 453 number of eddies seasonal cycle lags for by ~ 3 months from the winds, while the cEddy_{amp}^+
 454 is on phase with the winds and the maximum of trapped waves (winter; Zamudio et al.,
 455 2006), and the cEddy_{amp}^- could be a consequence of eddy-eddy interactions.

462 The reconstruction of the coherent eddies and their statistics have revealed regions
 463 with important coherent eddy contributions and a distinct seasonal evolution of the co-
 464 herent eddies. Remarkably, western boundary currents generate eddies through the in-

465 stability of the main currents and the seasonal cycle of coherent eddies, CEKE, and thus
 466 EKE could be associated with an inverse energy cascade observable through lagged sea-
 467 sonal cycles in the coherent eddy statistics. In addition to this, the amplitude of the sea-
 468 sonal cycle in the boundary currents is two times larger than any other region, thus the
 469 seasonality of the coherent eddies in boundary currents dominate the hemispherical sea-
 470 sonal cycle. Furthermore, the seasonal lag of the inverse energy cascade is coupled with
 471 the presence of fronts, such is the case of western boundary currents, and our results are
 472 consistent with the notion of baroclinic instability generating eddies and through eddy-
 473 eddy interactions an lagged inverse energy cascade.

474 7 Summary and Conclusions

475 We investigated the coherent eddy kinetic energy, its seasonal cycle, and the sea-
 476 sonal cycle of coherent eddy properties. Half of the EKE is explained by coherent ed-
 477 dies. Furthermore, the seasonal cycle of the satellite geostrophic EKE and CEKE is likely
 478 a consequence of eddy-eddy interactions and the inverse energy cascade.

479 This result appears to be consistent with ... Although the coherent eddy seasonal
 480 cycle could be a consequence of multiple factors, such as ..., there is evidence to sug-
 481 gest Generally, ...

482 Acknowledgments

483 Chelton & Schlax (2013) dataset was produced by SSALTO/DUACS and distributed by
 484 AVISO+ (<https://www.aviso.altimetry.fr/>) with support from CNES, developed
 485 and validated in collaboration with E.Mason at IMEDEA. Global coherent eddy recon-
 486 struction, coherent and non-coherent eddy kinetic energy datasets, in addition to grid-
 487 ded coherent eddy tracking datasets are publicly available at (<https://doi.org/10.5281/zenodo.4646429>). All analyses and figures in this manuscript are reproducible via Jupyter
 488 notebooks and instructions can be found in the Github repository `CEKE_climatology`
 489 (https://github.com/josuemtzmo/CEKE_climatology). Trends used the Python Pack-
 490 age `xarrayMannKendall` (<https://doi.org/10.5281/zenodo.4458776>)

492 References

- 493 Arbic, B. K., Polzin, K. L., Scott, R. B., Richman, J. G., & Shriver, J. F. (2013).
 494 On Eddy Viscosity, Energy Cascades, and the Horizontal Resolution of Gridded

- 495 Satellite Altimeter Products*. *Journal of Physical Oceanography*, 43(2), 283–300.
496 doi: 10.1175/jpo-d-11-0240.1
- 497 Ashkezari, M. D., Hill, C. N., Follett, C. N., Forget, G., & Follows, M. J. (2016).
498 Oceanic eddy detection and lifetime forecast using machine learning methods.
499 *Geophysical Research Letters*, 43(23). doi: 10.1002/2016gl071269
- 500 Beron-Vera, F. J., Wang, Y., Olascoaga, M. J., Goni, G. J., & Haller, G. (2013). Ob-
501 jective Detection of Oceanic Eddies and the Agulhas Leakage. *Journal of Physical
502 Oceanography*, 43(7), 1426–1438. doi: 10.1175/JPO-D-12-0171.1
- 503 Bouali, M., Sato, O. T., & Polito, P. S. (2017). Temporal trends in sea surface tem-
504 perature gradients in the South Atlantic Ocean. *Remote Sensing of Environment*,
505 194, 100–114. doi: 10.1016/j.rse.2017.03.008
- 506 Callies, J., Flierl, G., Ferrari, R., & Fox-Kemper, B. (2015). The role of mixed-layer
507 instabilities in submesoscale turbulence. *Journal of Fluid Mechanics*, 788, 5–41.
508 doi: 10.1017/jfm.2015.700
- 509 Cane, M. A., Clement, A. C., Kaplan, A., Kushnir, Y., Pozdnyakov, D., Seager, R.,
510 ... Murtugudde, R. (1997). Twentieth-Century Sea Surface Temperature Trends.
511 *Science*, 275(5302), 957–960. doi: 10.1126/science.275.5302.957
- 512 Chaudhuri, A. H., Gangopadhyay, A., & Bisagni, J. J. (2009). Interannual variabil-
513 ity of Gulf Stream warm-core rings in response to the North Atlantic Oscillation.
514 *Continental Shelf Research*, 29(7), 856–869. doi: 10.1016/j.csr.2009.01.008
- 515 Chelton, D. B., Gaube, P., Schlax, M. G., Early, J. J., & Samelson, R. M. (2011).
516 The influence of nonlinear mesoscale eddies on near-surface oceanic chlorophyll.
517 *Science*, 334(6054), 328-32. doi: 10.1126/science.1208897
- 518 Chelton, D. B., & Schlax, M. G. (2013). *Mesoscale eddies in altimeter observations
519 of ssh*.
- 520 Chelton, D. B., Schlax, M. G., Samelson, R. M., & de Szoeke, R. A. (2007). Global
521 observations of large oceanic eddies. *Geophysical Research Letters*, 34(15),
522 L15606. doi: 10.1029/2007GL030812
- 523 CMEMS. (2017). The Ssalto/Duacs altimeter products were produced and dis-
524 tributed by the Copernicus Marine and Environment Monitoring Service. *Aviso
525 Dataset*. Retrieved from <https://www.aviso.altimetry.fr/>
- 526 Cui, W., Wang, W., Zhang, J., & Yang, J. (2020). Identification and census statis-
527 tics of multicore eddies based on sea surface height data in global oceans. *Acta*

- 528 *Oceanologica Sinica*, 39(1), 41–51. doi: 10.1007/s13131-019-1519-y
- 529 Faghmous, J. H., Frenger, I., Yao, Y., Warmka, R., Lindell, A., & Kumar, V. (2015,
530 6). A daily global mesoscale ocean eddy dataset from satellite altimetry. *Scientific
531 Data*, 2, 150028 EP -. doi: 10.1038/sdata.2015.28
- 532 Ferrari, R., & Wunsch, C. (2009). Ocean Circulation Kinetic Energy: Reservoirs,
533 Sources, and Sinks. *Annual Review of Fluid Mechanics*, 41(1), 253–282. doi: 10
534 .1146/annurev.fluid.40.111406.102139
- 535 Frenger, I., Gruber, N., Knutti, R., & Münnich, M. (2013). Imprint of Southern
536 Ocean eddies on winds, clouds and rainfall. *Nature Geoscience*, 6(8), 608 EP -.
537 doi: 10.1038/ngeo1863
- 538 Frenger, I., Münnich, M., Gruber, N., & Knutti, R. (2015). Southern Ocean eddy
539 phenomenology. *Journal of Geophysical Research: Oceans*, 120(11), 7413-7449.
540 doi: 10.1002/2015JC011047
- 541 Fu, L., Chelton, D., Le Traon, P., & Oceanography, M. R. (2010). Eddy dynamics
542 from satellite altimetry. *Oceanography*, 23(4), 14-25. doi: 10.2307/24860859
- 543 Gill, A., Green, J., & Simmons, A. (1974). Energy partition in the large-scale ocean
544 circulation and the production of mid-ocean eddies. *Deep Sea Res Oceanogr Abstr*,
545 21(7), 499-528. doi: 10.1016/0011-7471(74)90010-2
- 546 Hogg, A. M., & Blundell, J. R. (2006). Interdecadal variability of the southern
547 ocean. *Journal of Physical Oceanography*, 36(8), 1626-1645. doi: 10.1175/
548 JPO2934.1
- 549 Hogg, A. M., Meredith, M. P., Chambers, D. P., Abrahamsen, E. P., Hughes,
550 C. W., & Morrison, A. K. (2015). Recent trends in the Southern Ocean
551 eddy field. *Journal of Geophysical Research: Oceans*, 120(1), 257-267. doi:
552 10.1002/2014JC010470
- 553 Hu, S., Sprintall, J., Guan, C., McPhaden, M. J., Wang, F., Hu, D., & Cai,
554 W. (2020, 2). Deep-reaching acceleration of global mean ocean circula-
555 tion over the past two decades. *Science Advances*, 6(6), eaax7727. doi:
556 10.1126/sciadv.aax7727
- 557 Japan Meteorological Agency, Japan. (2013). *Jra-55: Japanese 55-year reanalysis,
558 daily 3-hourly and 6-hourly data*. Boulder CO: Research Data Archive at the Na-
559 tional Center for Atmospheric Research, Computational and Information Systems
560 Laboratory. Retrieved from <https://doi.org/10.5065/D6HH6H41>

- 561 Kang, D., & Curchitser, E. N. (2017). On the Evaluation of Seasonal Variability of
562 the Ocean Kinetic Energy. *Geophysical Research Letters*, 47, 1675-1583. doi: 10
563 .1175/JPO-D-17-0063.1
- 564 Li, G., Cheng, L., Zhu, J., Trenberth, K. E., Mann, M. E., & Abraham, J. P. (2020).
565 Increasing ocean stratification over the past half-century. *Nature Climate Change*,
566 1–8. doi: 10.1038/s41558-020-00918-2
- 567 Martínez-Moreno, J., Hogg, A. M., England, M., Constantinou, N. C., Kiss, A. E.,
568 & Morrison, A. K. (2021). Global changes in oceanic mesoscale currents over the
569 satellite altimetry record. *Journal of Advances in Modeling Earth Systems*, 0(ja).
570 doi: 10.1029/2019MS001769
- 571 Martínez-Moreno, J., Hogg, A. M., Kiss, A. E., Constantinou, N. C., & Morrison,
572 A. K. (2019). Kinetic energy of eddy-like features from sea surface altimeter.
573 *Journal of Advances in Modeling Earth Systems*, 11(10), 3090-3105. doi:
574 10.1029/2019MS001769
- 575 Patel, R. S., Llort, J., Strutton, P. G., Phillips, H. E., Moreau, S., Pardo, P. C.,
576 & Lenton, A. (2020). The Biogeochemical Structure of Southern Ocean
577 Mesoscale Eddies. *Journal of Geophysical Research: Oceans*, 125(8). doi:
578 10.1029/2020jc016115
- 579 Pilo, G. S., Mata, M. M., & Azevedo, J. L. L. (2015). Eddy surface properties and
580 propagation at Southern Hemisphere western boundary current systems. *Ocean
581 Science*, 11(4), 629–641. doi: 10.5194/os-11-629-2015
- 582 Qiu, B. (1999). Seasonal Eddy Field Modulation of the North Pacific Subtropical
583 Countercurrent: TOPEX/Poseidon Observations and Theory. *Journal of Physical
584 Oceanography*, 29(10), 2471–2486. doi: 10.1175/1520-0485(1999)029<2471:sefmot>2
585 .0.co;2
- 586 Qiu, B., & Chen, S. (2004). Seasonal Modulations in the Eddy Field of the South
587 Pacific Ocean. *Journal of Physical Oceanography*, 34(7), 1515–1527. doi: 10.1175/
588 1520-0485(2004)034<1515:smitef>2.0.co;2
- 589 Qiu, B., Chen, S., Klein, P., Sasaki, H., & Sasai, Y. (2014). Seasonal Mesoscale
590 and Submesoscale Eddy Variability along the North Pacific Subtropical Coun-
591 tercurrent. *Journal of Physical Oceanography*, 44(12), 3079–3098. doi:
592 10.1175/JPO-D-14-0071.1
- 593 Ruela, R., Sousa, M. C., deCastro, M., & Dias, J. M. (2020). Global and regional

- 594 evolution of sea surface temperature under climate change. *Global and Planetary*
595 *Change*, 190, 103190. doi: 10.1016/j.gloplacha.2020.103190
- 596 Sasaki, H., Klein, P., Qiu, B., & Sasai, Y. (2014). Impact of oceanic-scale inter-
597 actions on the seasonal modulation of ocean dynamics by the atmosphere. *Nature*
598 *Communications*, 5(1), 5636. doi: 10.1038/ncomms6636
- 599 Schubert, R., Schwarzkopf, F. U., Baschek, B., & Biastoch, A. (2019). Submesoscale
600 Impacts on Mesoscale Agulhas Dynamics. *Journal of Advances in Modeling Earth*
601 *Systems*, 11(8), 2745–2767. doi: 10.1029/2019ms001724
- 602 Siegel, D., Peterson, P., DJ, M., Maritorena, S., & Nelson, N. (2011). Bio-optical
603 footprints created by mesoscale eddies in the Sargasso Sea. *Geophysical Research*
604 *Letters*, 38(13), n/a-n/a. doi: 10.1029/2011GL047660
- 605 Uchida, T., Abernathey, R., & Smith, S. (2017). Seasonality of eddy kinetic energy
606 in an eddy permitting global climate model. *Ocean Modelling*, 118, 41-58. doi: 10
607 .1016/j.ocemod.2017.08.006
- 608 Wunsch, C. (2020). Is The Ocean Speeding Up? Ocean Surface Energy Trends.
609 *Journal of Physical Oceanography*, 50(11), 1–45. doi: 10.1175/jpo-d-20-0082.1
- 610 Wunsch, C., & Ferrari, R. (2004). Vertical mixing, energy, and the general circula-
611 tion of the oceans. *Annual Review of Fluid Mechanics*, 36(1), 281–314. doi: 10
612 .1146/annurev.fluid.36.050802.122121
- 613 Wyrtki, K., Magaard, L., & Hager, J. (1976). Eddy energy in the oceans. *Journal of*
614 *Geophysical Research*, 81(15), 2641-2646. doi: 10.1029/JC081i015p02641
- 615 Yue, S., & Wang, C. (2004). The Mann-Kendall Test Modified by Effective Sample
616 Size to Detect Trend in Serially Correlated Hydrological Series. *Water Resources*
617 *Management*, 18(3), 201–218. doi: 10.1023/b:warm.0000043140.61082.60
- 618 Zamudio, L., Hurlburt, H. E., Metzger, E. J., Morey, S. L., O'Brien, J. J., Tilburg,
619 C., & Zavala-Hidalgo, J. (2006). Interannual variability of Tehuantepec ed-
620 dies. *Journal of Geophysical Research: Oceans (1978–2012)*, 111(C5). doi:
621 10.1029/2005JC003182